ACS APPLIED ENERGY MATERIALS

www.acsaem.org Article

$WO_3/BiVO_4$ Photoanodes: Facets Matching at the Heterojunction and $BiVO_4$ Layer Thickness Effects

Ivan Grigioni,[§] Giovanni Di Liberto,[§] Maria Vittoria Dozzi, Sergio Tosoni, Gianfranco Pacchioni, and Elena Selli*

Cite This: *ACS Appl. Energy Mater.* 2021, 4, 8421−8431 Read Online

ACCESS | Metrics & More | Article Recommendations | Supporting Information

ABSTRACT: Photoelectrochemical solar energy conversion offers a way to directly store light into energy-rich chemicals. Photoanodes based on the $WO_3/BiVO_4$ heterojunction are most effective mainly thanks to the efficient separation of photogenerated charges. The $WO_3/BiVO_4$ interfacial space region in the heterojunction is investigated here with the increasing thickness of the $BiVO_4$ layer over a WO_3 scaffold. On the basis of X-ray diffraction analysis results, density functional theory simulations show a $BiVO_4$ growth over the WO_3 layer along the $BiVO_4$ {010} face, driven by the formation of a stable interface with new covalent bonds, with a favorable band alignment and band bending between the two oxides. This crystal facet phase matching allows a smooth transition between the electronic states of the two oxides and may be a key factor ensuring the high efficiency attained with this heterojunction. The photoelectrochemical activity of the $WO_3/BiVO_4$ photoanodes depends on both the irradiation wavelength and the thickness of the visible-light-absorbing $BiVO_4$ layer, a 75 nm thick $BiVO_4$ layer on WO_3 being best performing.

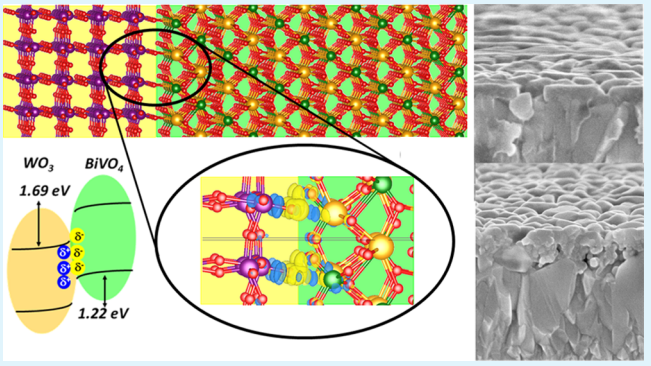

KEYWORDS: *photoelectrochemistry, semiconductor interface, band alignment, density functional theory, WO_3, $BiVO_4$*

1. INTRODUCTION

Photoelectrochemical (PEC) water splitting is a promising route to directly generate hydrogen from water and solar light, and hydrogen is regarded as a clean energy vector, enabling the storage of the intermittent renewable solar energy. A solar-to-hydrogen (STH) conversion efficiency of 10% is considered as a threshold for industrialization.[1] Photoanodes for the oxygen evolution reaction (OER) based on metal oxides offer good stability and light harvesting over the whole visible spectrum.[2−5]

In this scenario, $BiVO_4$ rapidly emerged as one of the most promising visible-light-active photoanode materials. State-of-the-art $BiVO_4$ electrodes display remarkable stability above 1000 h[6,7] and a STH conversion efficiency of 5%.[8] The deposition of OER catalysts allows to decrease the overpotential needed to speed up the slow O_2 evolution kinetics, thus boosting the electrode performance.[9−11] However, a full utilization of the photons absorbed by $BiVO_4$ is hampered by the recombination of photogenerated charges and several strategies, such as doping,[12−15] gradient doping,[8] reduction by H_2 treatment,[16] and heterojunction engineering,[17] have been developed to mitigate such a detrimental energy loss path.

Photoanodes based on the $WO_3/BiVO_4$ heterojunction showed a record STH conversion efficiency[18,19] owing to the beneficial combination of the excellent visible-light-harvesting properties of $BiVO_4$ and the superior electron conductivity of WO_3.[20−22] Indeed, resistance to charge transfer largely diminishes when $BiVO_4$ is combined with WO_3, as demonstrated by electrochemical impedance spectroscopy measurements.[17] Furthermore, the in-built electric field generated by the favorable band energy offset between the two oxides[23] drives efficient separation of photogenerated electron−hole pairs since holes remain in the $BiVO_4$ valence band (VB),[24,25] while photopromoted electrons flow into the lower-lying WO_3 conduction band (CB), where they rapidly diffuse to the external circuit, exploiting the better charge mobility within this material.[26] This enhanced spatial charge separation occurring in $WO_3/BiVO_4$ heterojunctions leads to relatively long-living charge carriers[27,28] and to efficient light harvesting.[18,19]

Although the complex charge-carrier dynamics in this system has been studied by different groups in very recent years,[24,28−32] the crystal growth of $BiVO_4$ at the interface

Received: June 7, 2021
Accepted: July 30, 2021
Published: August 12, 2021

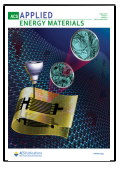

https://doi.org/10.1021/acsaem.1c01623
ACS Appl. Energy Mater. 2021, 4, 8421−8431

with WO_3 during the heterojunction formation, which may have a key role in determining the outstanding charge separation of this architecture, is so far little explored. A recent study reveals, however, that the crystallographic orientation of the underlying WO_3 layer may affect the PEC performance of $WO_3/BiVO_4$ heterojunctions.[33]

In the present work, we investigate the effect that the thickness of the visible-light-absorbing $BiVO_4$ layer has on the PEC performance of the photoanodes, further complementing the experimental results with first-principles calculations. In particular, two series of six photoanodes were prepared through a wet chemistry synthetic method. The first series consists of $BiVO_4$ layers of variable thicknesses directly deposited on a fluorine-doped tin oxide (FTO) conductive glass, while the second one was obtained by the deposition of the same $BiVO_4$ layers on a WO_3 layer supported on FTO. In both series, only the thickness of the $BiVO_4$ layer was varied while maintaining that of WO_3 fixed. The morphological and crystallographic features of the two photoanode series were investigated in relation to their PEC performance. Density functional theory (DFT) simulations allowed us to identify specific facet interaction between the two oxides, which may guide and control the progressive crystalline growth at the heterojunction and create a stable interface with a type-II band alignment. In addition, the formation of an interface polarization in the contact region between the two oxides leads to a band bending that favors charge-carrier separation.

2. EXPERIMENTAL SECTION

2.1. Materials. The following chemicals were employed: tungsten(VI) ethoxide 99.8% (5% w/v in ethanol), ammonium vanadium oxide, bismuth(III) nitrate pentahydrate ACS 98%, benzyl alcohol ACS 99% (Alpha Aesar), ethyl cellulose (MP Biomedics), citric acid 99% and zirconium oxynitrate hydrate 99% (Aldrich), and anhydrous sodium sulfate (Fisher Scientific).

2.2. Photoelectrode Preparation. The WO_3 layer was prepared as follows: 1.0 mL of tungsten ethoxide, 5 wt % in ethanol, was added to 42 mg of citric acid acting as a stabilizer. Once citric acid was completely dissolved, benzyl alcohol (0.3 mL) and ethyl cellulose (40 mg) were added to the solution and stirred overnight to allow the complete dissolution of ethyl cellulose. The so-obtained paste is stable for several weeks. FTO glass (Pilkington Glass, TEC-7, thickness 2 mm) was coated with the paste by spin-coating at 4000 rpm for 30 s. The final spinning rate was reached with a three acceleration step program: 200 rpm s^{-1} up to 1000 rpm, then 500 rpm s^{-1} up to 2000 rpm, and finally 2000 rpm s^{-1} up to 4000 rpm. Prior to deposition, the FTO glass was cleaned by a 30 min long sonication in an aqueous soap solution, then in ethanol, and finally in water. After coating, the film was dried at 80 °C for 1 h and then annealed at 500 °C for 8 h.

Bismuth vanadate films were prepared starting from a liquid solution similar to that reported elsewhere.[34] In a typical synthesis, 0.002 mol of $Bi(NO_3)_3$ and NH_4VO_3 were added to 6 mL of HNO_3 23.3% containing 0.004 mol citric acid. The mixture was stirred overnight to allow dissolution of the precursor. The $BiVO_4$-based photoanodes were prepared on clean FTO by spinning the solution at 8000 rpm for 30 s with an acceleration rate of 6000 rpm s^{-1}. The film was then dried for 1 h at 80 °C and calcined for 1 h at 500 °C. The thickness of the $BiVO_4$ film was controlled by depositing successive coating layers by repeating the spin-coating procedure and the thermal treatment up to eight times. Once the desired optical density of the film was obtained, the electrode was annealed at 500 °C for 8 h.

The $WO_3/BiVO_4$ combined photoanodes with different thicknesses were prepared by coating the WO_3 electrodes (prepared as described above) with the $BiVO_4$ precursor solution. Then, the composite film was dried at 80 °C for 1 h and annealed at 500 °C for 1 h. The amount of $BiVO_4$ in the $WO_3/BiVO_4$ electrodes was controlled in the same way as for the $BiVO_4$ photoanode series. The films were finally annealed at 500 °C for 8 h.

Using the here described successive $BiVO_4$ layer deposition technique, we effectively tailored the thickness of the $BiVO_4$ compart, obtaining a comparable $BiVO_4$ thickness in the $BiVO_4$ and $WO_3/BiVO_4$ electrodes prepared by applying the same number of coated layers (the same optical densities were obtained in the wavelength region where only $BiVO_4$ absorbs light). The two series of photoanodes were labeled as $BiVO_4$-*X* and $WO_3/BiVO_4$-*X*, with *X* indicating the $BiVO_4$ layer thickness expressed in nanometers (X = 15, 30, 50, 75, 115, and 160). Each actual $BiVO_4$ thickness value was slightly approximated to simplify the direct comparison between the films of the two series containing the same number of $BiVO_4$-coated layers. Please refer to Table S1 of the Supporting Information for the exact film thickness values.

A zirconia film deposited on FTO, prepared starting from $ZrO(NO_3)_2$ with a procedure similar to that employed for the preparation of $BiVO_4$ films (i.e., same precursors concentration, deposition rate, and annealing temperature) was employed, instead of FTO, to record the baseline when recording the absorption spectra of the $FTO/BiVO_4$ photoanode series in the transmittance mode. In fact, when FTO was employed to record the baseline, negative absorbance values were obtained for the thinner $FTO/BiVO_4$ electrodes due to considerable light scattering by pristine FTO, exhibiting an average absorbance of ca. 0.2 above 400 nm. On the other hand, upon covering FTO with the wide band gap thin ZrO_2 layer, this scattering phenomenon significantly decreased.

2.3. Optical, Morphological, and Structural Characterization. Images showing the morphology and the cross-sectional view of the electrodes were obtained using a FEI Magellan-400 field emission scanning electron microscope. UV−visible absorption spectra were recorded using a Jasco V650 spectrophotometer. The crystalline phase of the materials was determined through X-ray diffraction (XRD) analysis using a Philips PW1820 instrument with Cu Kα radiation at 40 mA and 40 kV. The diffractograms were base-corrected employing Origin software.

2.4. PEC Characterization. PEC measurements were carried out using a three-electrode cell with an Ag/AgCl (3.0 M NaCl) reference electrode, a platinum gauze as a counter electrode, and a Princeton Applied Research 2263 (PARstat) potentiostat. The light source was a 300 W Xe lamp with an AM 1.5 G illumination (1 sun). A 0.5 M Na_2SO_4 aqueous solution was used in electrochemical measurements. The potential versus Ag/AgCl was converted into the RHE scale using the following equation: $E_{RHE} = E_{AgCl} + 0.059\ pH + E_{AgCl}^{\circ}$, with E_{AgCl}° (3.0 M NaCl) = 0.210 V at 25 °C. Linear sweep voltammetry (LSV) scans were recorded at 10 mV s^{-1} under backside irradiation (irradiation on the FTO side), starting from the open-circuit potential after 5 min of irradiation, up to 1.8 V versus RHE.

Incident photon-to-current efficiency (IPCE) measurements were carried out with a setup similar to that used for PEC experiments, with a Bausch and Lomb grating monochromator placed between the Xe lamp and the sample. A 1.23 V bias versus NHE was applied and the current was measured with a 10 nm step, within the 350−600 nm wavelength range. The incident light power was measured at each wavelength using a calibrated photodiode connected to a Keithley 617 electrometer. The IPCE was calculated at each wavelength λ (nm) using the following equation

$$\mathrm{IPCE} = \frac{1240 \times J}{P_\lambda \times \lambda} \times 100$$

where J is the photocurrent density (mA cm^{-2}) and P_λ (mW cm^{-2}) is the power of the monochromatic light at the specific wavelength λ.

2.5. Computational Methods. Calculations were performed at the DFT level by means of the CRYSTAL code.[35] For the exchange and correlation potential, we recurred to the HSE06 range-separated hybrid functional (25% fraction of Fock exchange),[36] a suitable choice for the treatment of solids.[37,38] The all-electron Gaussian-type basis sets 8-411(d1) and 86-411(d31) were adopted for O and V.[39] For the heavy tungsten and bismuth atoms, we adopted the effective core pseudopotential (ECP) by Hay and Wadt, with a modified double-

https://doi.org/10.1021/acsaem.1c01623
ACS Appl. Energy Mater. 2021, 4, 8421−8431

zeta basis set for valence electrons.[40,41] The valence electrons treated explicitly are 5p, 6s, and 5d for W and 6s and 6p for Bi. These basis sets were already used and benchmarked for the study of these materials.[42−44] In particular, the adopted basis set of WO_3 has been used and discussed in extended studies conducted on both bulk and surfaces in the past.[42,43] In the case of $BiVO_4$, we benchmarked the performances of the adopted basis sets against available flexible TZVP basis functions.[45] The impact on the electronic band gaps of bulk phases induces differences as high as 0.1 eV and only 0.1% on the lattice parameters. Bulk, surface, and interface models were fully optimized. Full details on cutoff limits, convergence criteria and thresholds, and reciprocal space sampling are reported in the Supporting Information.

The choice of the functional used and the mismatch induced in forming a heterojunction are among the approximations that affect the absolute values of the computed properties. About the first point, it should be mentioned that the $BiVO_4$ band gap computed with hybrid functionals is overestimated.[38,46] This opens the question of the functional to be used for the $WO_3/BiVO_4$ junction. In a seminal study on the band alignment in ZnO/TiO_2, Conesa used the average value between the optimal exchange fractions derived for the isolated ZnO and TiO_2 components.[47] This strategy performs well in general. However, the optimal exchange fractions to reproduce the experimental band gap of $BiVO_4$ and WO_3 are ∼0% and ∼0.22, respectively, and the average value for the heterostructure should be ∼0.1. This could result in very different band alignments for the real $BiVO_4/WO_3$ interface and for that derived for the independent species. Another strategy consists in using the same DFT functional for the separated components and the heterojunction. This procedure leads to an error that is transferrable from independent units' calculations to heterojunction ones and therefore can be better rationalized. We adopted this second strategy.

The problem of mismatch has been studied in detail in this and other studies, with the observation that a strain of the entity present in our systems can result in about 0.2 eV error in the position of the band edges. In the present case, the adopted simulation cell implies lattice mismatches of 1.2 and 2.1% on *a* and *b* lattice vectors, respectively, leading to deviations of up to 0.1 eV in the position of the band edges. This is not going to affect the conclusions of this work. It is worth recalling that the simulation of interface models of this type with DFT methods implies the approximation that the structure of the interface is sharp to obey to the periodic boundary conditions, that is, dislocation and amorphization effects are not included in the simulation.

3. RESULTS AND DISCUSSION

3.1. Morphological, Optical, and Structural Characterization. Side-view field emission scanning electron microscopy (FESEM) images of the $BiVO_4$ photoanodes obtained upon the deposition of two and four $BiVO_4$-coated layers and that of the FTO glass used as support, together with those of the corresponding $WO_3/BiVO_4$ photoanodes and of the WO_3 photoanode, are reported in Figure 1.

Figure 1A shows that the asperities of the underlying FTO conductive glass still emerge from the thinnest $BiVO_4$ film in the $BiVO_4$-30 photoanode, while they are completely covered upon further deposition of two $BiVO_4$ layers in $BiVO_4$-75 (Figure 1B). On the other hand, the deposition of a ca. 200 nm thick WO_3 layer on FTO led to a flat surface (Figure 1F), and the deposition of only two $BiVO_4$ layers ensured a homogeneous coverage of the FTO/WO_3 underlying film in the $WO_3/BiVO_4$-30 photoanode (Figure 1D), while larger crystallites were obtained upon the deposition of four $BiVO_4$ layers onto WO_3 (see the image referring to $WO_3/BiVO_4$-75 in Figure 1E). In both photoanode series, successive $BiVO_4$ depositions led to an increase in size of the $BiVO_4$ grains, forming a mesoporous architecture.

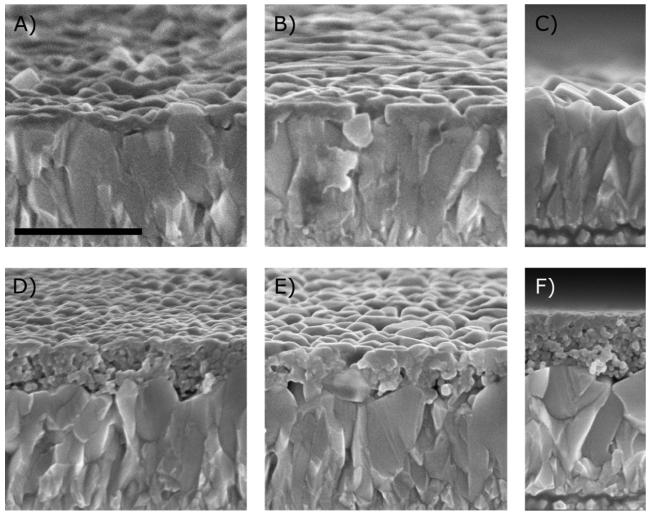

Figure 1. FESEM side-view images of the photoanodes obtained by the successive deposition of (A,D) two and (B,E) four $BiVO_4$ layers, (A,B) directly on the FTO conductive glass (films $BiVO_4$-30 and $BiVO_4$-75, respectively), and (D,E) on a 200 nm thick WO_3 layer (films $WO_3/BiVO_4$-30 and $WO_3/BiVO_4$-75, respectively); representative cross sections of (C) the FTO and (F) the WO_3 on the FTO film. The scale bar is 500 nm.

The absorption spectra of the $BiVO_4$ photoanode series are reported in Figure 2A, together with their picture. The absorbance linearly increases with the number of $BiVO_4$-coated layers, as shown in the inset of Figure 2A. From the thickness of the two-, four-, and six-layered $BiVO_4$ films, evaluated from the cross-sectional images reported in Figure S1 of the Supporting Information, and the absorption spectra of these films, the absorption coefficient of $BiVO_4$ at 420 nm, α_{420} = 6.7 10^4 cm^{-1}, was calculated, as detailed in the Supporting Information. This value was employed to estimate the thickness of the $BiVO_4$ layer in $WO_3/BiVO_4$ photoanodes.

The absorption spectra of the WO_3, $BiVO_4$-160, and $WO_3/BiVO_4$-160 films are shown in Figure 2B. Notably, the successive spin-coating and annealing procedure ensured reproducible results in terms of absorbance and film thickness increase on both FTO and FTO/WO_3 substrates also after eight layer depositions, as indicated by the almost superimposed absorption profiles of the $BiVO_4$-160 and $WO_3/BiVO_4$-160 systems. Residual apparent light absorption above 520 nm is mainly due to lattice fringes and light scattering.

The powder XRD patterns recorded with the two photoanode series with variable $BiVO_4$ thickness are shown in Figure 3. The patterns of both individual materials fit well with monoclinic (JCPDS 05-0363 for WO_3)[48,49] and monoclinic scheelite (JCPDS 75-1867 for $BiVO_4$)[34] structures. The XRD reflections of pure monoclinic scheelite $BiVO_4$ peaking at 2θ ca. 19, 29, 31, 34.5, and 35.3° (Figure 3A) correspond to the {110}, {121}, {040}, {200}, and {002} planes, and their intensities linearly increase with increasing $BiVO_4$ film thickness, as shown in Figure S2A. More specifically, the {040} reflex is associated to the $BiVO_4$ {010} crystal facet, which is known to be ∼0.1 J m^{-2} more stable than the {110} one.[50,51] These are known as the most stable monoclinic $BiVO_4$ surfaces.[52] Concerning the XRD patterns of the coupled $WO_3/BiVO_4$ systems reported in Figure 3B, the reflections assigned to monoclinic WO_3 (black squares at 2θ = 23.0, 24.3, and 34.1°) moderately decrease with the increasing number of

https://doi.org/10.1021/acsaem.1c01623
ACS Appl. Energy Mater. 2021, 4, 8421−8431

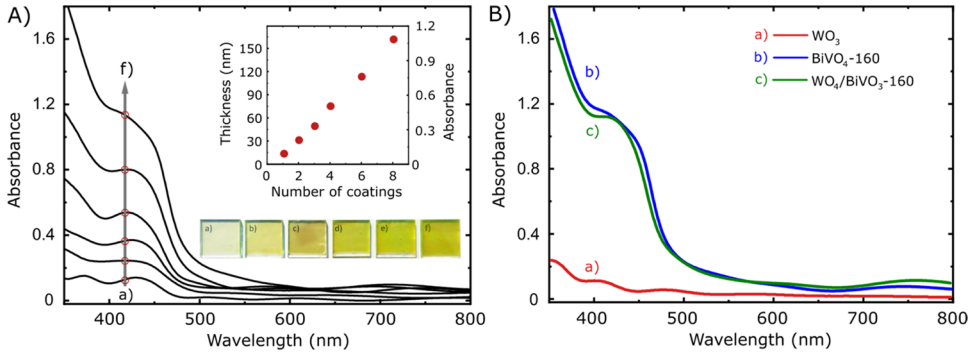

Figure 2. (A) Absorption spectra of the $BiVO_4$ series obtained by the successive deposition of (from a to f) one, two, three, four, six, and eight $BiVO_4$-coated layers; insets: thickness and absorbance increase (left and right ordinate axis, respectively) vs the number of $BiVO_4$-coated layers and corresponding pictures of the photoanode series. (B) Absorption spectra of the oxide films deposited on FTO: (a) WO_3; (b) $BiVO_4$-160; and (c) $WO_3/BiVO_4$-160.

$BiVO_4$ layers as it progressively attenuates the incident X-rays onto the underlying WO_3. At the same time, no substantial change appears in the position of the XRD patterns belonging to scheelite $BiVO_4$, with peak intensities increasing with increasing $BiVO_4$ thickness.

However, when comparing the XRD patterns of the thickest $BiVO_4$ films in the two series (Figure 3C), we notice that in the coupled system, the $BiVO_4$ peaks at 2θ = 19, 34.5, and 35.3°, corresponding to the {110}, {200}, and {002} planes, respectively, are less intense with respect to those of the corresponding individual $BiVO_4$ film. Differently, the relatively more intense peaks at 29 and 31°, associated with the most stable facets ({121} and {040} planes) of the monoclinic $BiVO_4$ phase, are almost unaffected by the presence of the underlying WO_3 coating layer and their peaks almost totally overlap in the diffraction patterns of the two thickest films in the two series (Figure 3C).

This difference can be better appreciated in Figure 4, where each XRD peak intensity determined for the two investigated sample series is reported as a function of the number of $BiVO_4$-coated layers. Interestingly, the main differences in the pattern intensity pertain to the {110} and {200}/{002} planes (Figure 4A,B), while the {121} and {040} planes originate similar peak intensities in the two photoelectrode series (Figure 4C,D). Thus, the presence of the WO_3 layer appears to inhibit the $BiVO_4$ crystal growth along the {110} and {200}/{002} crystallographic directions, promoting a slightly alternative structural evolution, possibly due to an additional surface stabilization occurring between WO_3 itself and the {121} or {010} planar structures of $BiVO_4$. A similar behavior has been recently observed for the interface between $BiVO_4$ and graphitic carbon nitride (g-C_3N_4) with a preferential growth along specific directions, consequently enhancing and weakening selected XRD peaks.[53]

Aiming at better appreciating the selective WO_3-induced alteration of the $BiVO_4$ crystal growth, the ratios between the intensity of each $BiVO_4$ XRD peak and that of the almost unaltered {121} pattern were calculated for all individual and coupled electrodes with the same number of $BiVO_4$-coated layers. These data are collected in Table 1. Due to their extremely low intensity, such calculation could not be applied to the {200} and {002} $BiVO_4$ reflections.

Regardless of the $BiVO_4$ layer thickness, the {110}/{121} peak intensity ratios calculated for the $WO_3/BiVO_4$ electrodes are systematically ca. half those obtained for the corresponding individual $BiVO_4$ films, confirming that the crystal growth along the {110} direction is partly prevented by the presence of the WO_3 sublayer. Differently, the crystal growth of {010} planar structures appears to be unaffected by the underlying presence of WO_3. Thus, the structure and orientation of the substrate (in the present case, WO_3) may play a key role in controlling the phase or orientation of the subsequently deposited $BiVO_4$ layers, as previously reported, e.g., in the case of monophasic TiO_2 film deposition on $SrTiO_3$ by pulsed laser ablation.[54]

3.2. Electronic Structure of the Interface. Aiming at getting further insights into the origin of the observed XRD peaks intensity mismatch in the two photoanode series, computational simulations were performed to shed light on (i) the nature and stability of the heterojunction at the sub-nanometer level, based on beneficial matching effects between specific crystalline facets of the two oxides, and (ii) the band edge alignment and band bending between WO_3 and $BiVO_4$.

We started from the experimental crystal structures of monoclinic WO_3 and $BiVO_4$.[55,56] The calculated lattice vectors of WO_3 are a = 7.345 Å, b = 7.617 Å, c = 7.816 Å, and β = 90.5° and compare well with the available experimental ones, a = 7.306 Å, b = 7.540 Å, c = 7.692 Å, and β = 90.9°.[55] The $BiVO_4$ crystal structure can be modeled employing two different settings, a body-centered $C2/c$ cell, space group no. 15, or a $I2/b$ one.[50,56,57] In the first case, the experimental crystal structure is described by the lattice parameters a = 7.258 Å, b = 11.706 Å, c = 5.084 Å, and β = 134.1°.[50,56,57] In the second one, the lattice parameters are a = 5.194 Å, b = 5.090 Å, c = 11.697 Å, and γ = 90.4°.[56,58] In our simulations, we adopted the first scheme. The calculated (HSE06) lattice parameters a, b, c, and β of WO_3 are 7.345 Å, 7.617 Å, 7.816 Å, and 90.5°, respectively. Those of $BiVO_4$ are 7.215 Å, 11.544 Å, 5.093 Å, and 134.9°, respectively (deviations from the experimental values are within 1.5%, see also the Supporting Information). Then, we cut the WO_3 and $BiVO_4$ most stable surfaces starting from the relaxed bulk structures, namely, a 1.6 nm thick WO_3 {001} slab and a 3.3 nm thick $BiVO_4$ {010} slab (see Table S3 for lattice parameters).[46,50,51,59] The convergence of the surface properties was checked against the size of the slab models.

A problem that arises when building an interface between two crystalline structures is that of the mismatch, which must be minimized to avoid spurious effects. We found that a 45° rotated {010} $BiVO_4$ supercell displays excellent matching with

https://doi.org/10.1021/acsaem.1c01623
ACS Appl. Energy Mater. 2021, 4, 8421−8431

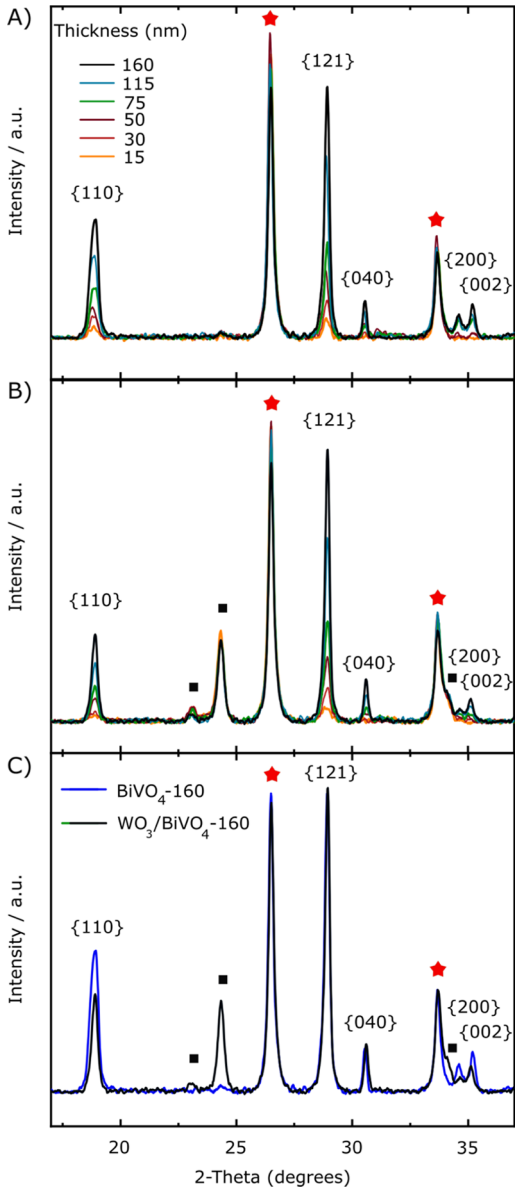

Figure 3. XRD analysis of (A) the $BiVO_4$ and (B) the $WO_3/BiVO_4$ photoanode series with different $BiVO_4$ thicknesses. (C) Comparison between the XRD patterns of $BiVO_4$-160 and $WO_3/BiVO_4$-160 thickest films. Red stars and black squares mark FTO and WO_3 patterns, respectively. The $BiVO_4$ planes are indicated with their *hkl* index.

the WO_3 {001} one,[44] including a good cation−anion matching (see Figure 5a and Table S3). This result is in line with the recently reported preferential facet orientation of WO_3, also affecting the $BiVO_4$ growth and facets at the $WO_3/BiVO_4$ heterojunction.[30] The lattice mismatches are 1.2% and 2.1% for *a* and *b* lattice vectors, respectively, and induce a deviation of $BiVO_4$ and WO_3 electronic properties as high as 0.1 eV. Therefore, the induced mismatch can be considered low in this respect.

It must be considered that $BiVO_4$ may expose the (110) surface as well, although this surface is less stable than the (010) one.[50,51] Table S3 reports the calculated surface energy which is 0.08 J m^{-2} higher than for the (010) facet. The band gap is instead very similar (difference 0.1 eV) as a consequence of the use of size-converged slab models. The same table also

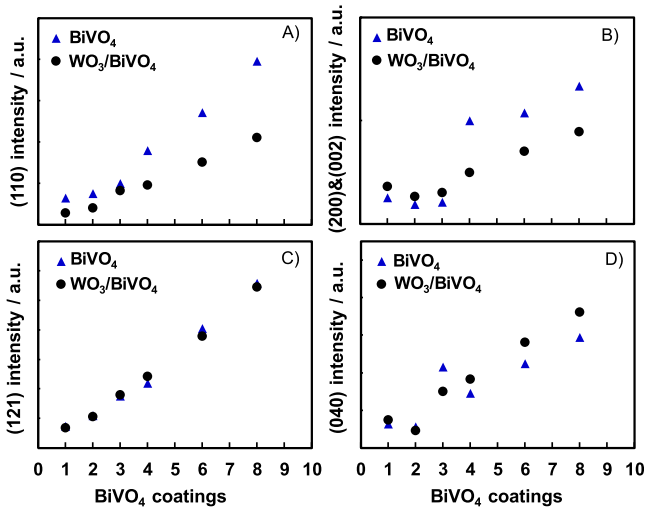

Figure 4. Calculated intensities of (A) {110}, (B) {200} and {002}, (C) {121}, and (D) {040} XRD reflections of $BiVO_4$ in both individual (blue triangles) and coupled (black circles) series samples as a function of the number of $BiVO_4$-coated layers.

Table 1. Relative Intensity of the {110} and {040} $BiVO_4$ XRD Reflections with Respect to the Almost Invariant {121} One, Calculated for Each Individual $BiVO_4$ and Corresponding $WO_3/BiVO_4$ Coupled Electrode with the Same Number of $BiVO_4$-Coated Layers

	{110}/{121}		{040}/{121}	
$BiVO_4$ coatings	$BiVO_4$	$WO_3/BiVO_4$	$BiVO_4$	$WO_3/BiVO_4$
1	0.88	0.43	0.17	0.22
2	0.69	0.38	0.10	0.09
3	0.57	0.46	0.25	0.17
4	0.82	0.40	0.13	0.15
6	0.67	0.40	0.11	0.15
8	0.71	0.39	0.11	0.13

reports the calculated lattice vectors. The (010) surface has a nearly square lattice (a = 5.036 Å, b = 5.202 Å, and γ = 90°), while the $BiVO_4$ (110) lattice is oblique, with a = 5.084 Å, b = 6.842 Å, and γ = 112.55°. This affects the possible lattice matching with WO_3 (001). Indeed, $BiVO_4$ (010) shows an excellent matching by taking a $(\sqrt{2})$, $(\sqrt{2})$ supercell, with mismatches equal to 1.1, 2.1, and 2.1% for *a*, *b*, and γ, respectively. We did several attempts to find a suitable lattice matching between $BiVO_4$ (110) and WO_3 (001), and we managed to design an interface lattice with an acceptable mismatch only by invoking very large supercells, where a 2 × 5 supercell of WO_3 (001) matches a rotated supercell of $BiVO_4$ (110) with lattice mismatches of 4.3, 2.5, and 0.8%. This cell should have lattice parameters equal to 14.620, 36.981, and 90 Å, and it is made by 2224 atoms. Unfortunately, such a large model results in too heavy computational demand at the HSE06 level. Based on stability and lattice mismatch considerations, we decided to focus on a $WO_3/BiVO_4$ interface where $BiVO_4$ exposes the (010) surface.

Upon full geometry optimization, new chemical bonds form at the interface, as evidenced in Figure 5b. In particular, Bi−O bonds (d = 2.73 Å) are preferentially formed, rather than V−O ones (d = 3.29 Å), while the W−O bond distance in the contact region (1.69 Å) is the same as in WO_3 (1.70 Å).

https://doi.org/10.1021/acsaem.1c01623
ACS Appl. Energy Mater. 2021, 4, 8421−8431

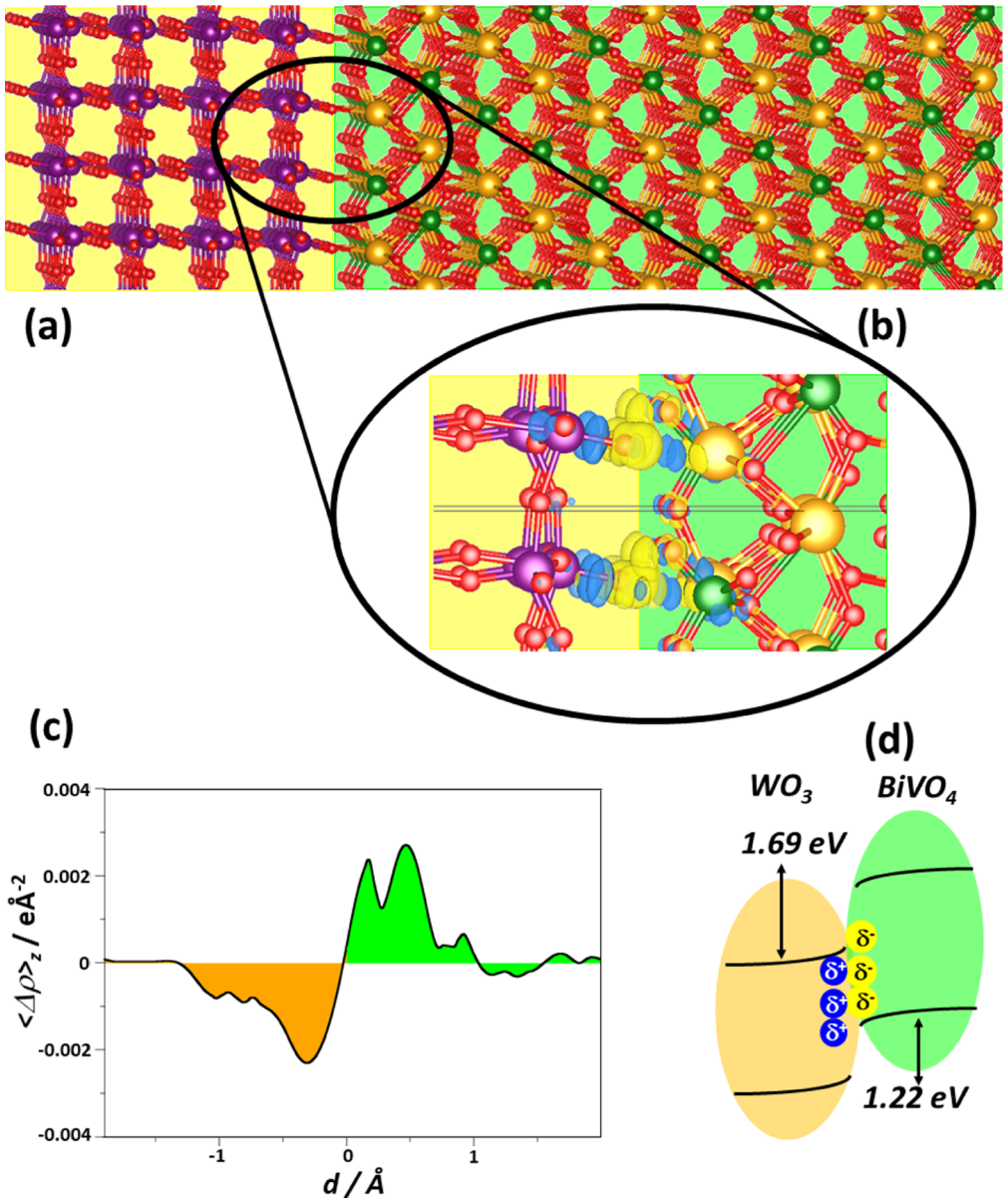

Figure 5. (a) Optimized $WO_3/BiVO_4$ interface model [left WO_3 (001), right $BiVO_4$ (010)]. (b) Magnified interface region which shows accumulation (yellow) and depletion (blue) regions from electron density difference ($\Delta\rho$) iso-surfaces (0.01 e Å^{-3}). (c) Averaged $\Delta\rho_z$ along planes with the same nonperiodic direction z. (d) Schematic view of the band alignment of the $WO_3/BiVO_4$ system according to the calculated VBOs and CBOs and interface polarization. Atoms labeling: purple: W; red: O; pink: V; and dark green: V. Orange- and light green-shaded areas surround WO_3 and $BiVO_4$ units.

The energetics of the interface was evaluated by calculating the interfacial energy (E_{form}), that is, the formation energy of the interface from the bulk materials.[60] E_{form} = 0.66 J m^{-2} indicates a high stability of the interface.[61] Furthermore, the formation of the interface from the separated WO_3 and $BiVO_4$ slabs implies an energy gain by 0.13 J m^{-2}, as evidenced by the calculated adhesion energy E_{ad}, defined as the energy of the interface minus that of the separated slabs.

Concerning the electronic properties, interface polarization and the band alignment of the $WO_3/BiVO_4$ interface, the calculated band gap of WO_3 is 2.98 eV, close to the experimental estimates (2.6−3.2 eV);[55,62] the band gap of $BiVO_4$ (3.23 eV) is overestimated by about 0.7 eV with respect to the experimental value but in line with calculated values with the same functional.[38,63] The band gaps of WO_3 (001) and $BiVO_4$ (010) slabs are 2.86 and 3.33 eV, thus almost converged to the bulks' values (see Table S3 for full details). We evaluated the interface polarization (Δq) and the direction of the band bending, an important aspect to determine the preferred location for photogenerated electrons and holes.[64,65] We estimated Δq in two different ways using the Mulliken charges and the charge density difference $\Delta\rho$, defined as $\Delta\rho = \rho_{WO_3/BiVO_4} - \rho_{WO_3} - \rho_{BiVO_4}$, and the integrated plane-averaged charge density difference $\langle\Delta\rho\rangle_z$. The two approaches give the same qualitative trend with Δq = 0.2 e nm^{-2} by using Mulliken charges and 0.1 e nm^{-2} by using $\langle\Delta\rho\rangle_z$. The analysis shows that an electron polarization occurs from WO_3 to $BiVO_4$ due to the interface formation (see also Figure 5c), which shows a charge depletion on WO_3 and a charge accumulation on $BiVO_4$.

https://doi.org/10.1021/acsaem.1c01623
ACS Appl. Energy Mater. 2021, 4, 8421−8431

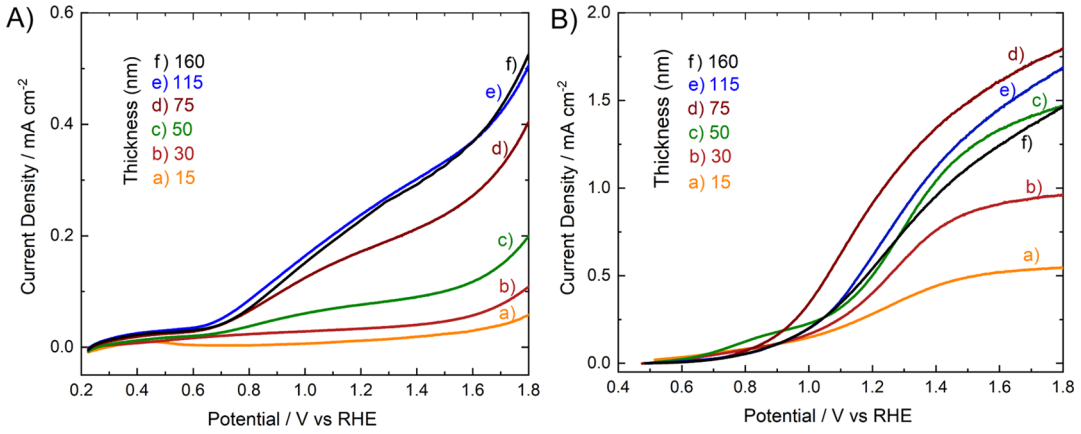

Figure 6. LSV curves under AM 1.5 G irradiation of (A) the $BiVO_4$ and (B) the $WO_3/BiVO_4$ photoanodes recorded under backside irradiation in 0.5 M Na_2SO_4 aqueous solutions.

The VB and CB offsets (VBOs, CBOs) (Figure 5d) were calculated following the potential line-up procedure used in previous works[47,66,67] and briefly described in the Supporting Information. The system is characterized by a type-II heterojunction, thus favorable for charge-carrier separation,[68−70] in line with Mott−Schottky analyses.[71]

The predicted type-II alignment is in line with the measured band edges of WO_3 and $BiVO_4$ materials[17] (Table S5). The interface formation is expected to be beneficial for carrier separation because both (i) band edge alignment and (ii) interface polarization suggest that photopromoted electrons should migrate from $BiVO_4$ to WO_3 and photogenerated holes in the opposite direction, thus providing a first-principles rationalization of the experimental observations.

The formation of the interface leads to a ∼0.3 eV enhancement of the band offsets, which is expected to improve the driving force of the electron migration toward WO_3 and holes migration toward $BiVO_4$. This 0.3 eV band offset increase is similar to that obtained in oxide interfaces.[72]

The convergence of the results as a function of the $BiVO_4$ layer thickness was investigated in order to exclude quantum confinement effects.[73] We simulated two additional interface models (full data in the Supporting Information) having different $BiVO_4$ thicknesses, while the thickness of WO_3 was kept fixed to 1.6 nm since it already leads to converged properties. We reduced the $BiVO_4$ thickness from 3.3 to 2.2 and 1.1 nm, respectively (see Table S4). Lattice constants and adhesion energies are very close in the three models. Also, the band alignment remains unchanged and the VBO and CBO deviate by less than 0.1 eV. Therefore, from a purely thermodynamic point of view, the electronic properties of $WO_3/BiVO_4$ are converged with a $BiVO_4$ film thickness of 2−3 nm, which is far below the thickness of the thinnest $BiVO_4$ layer (15 nm) in our photoanodes.

3.3. PEC Characterization. The LSV curves recorded under backside irradiation (irradiation on the FTO side) with individual $BiVO_4$ or with the corresponding coupled $WO_3/BiVO_4$ photoanodes with different $BiVO_4$ thicknesses can be compared in Figure 6 in terms of photocurrent density versus applied potential ($J-V$) plots.

The LSV response obtained from the heterojunction photoanodes was much higher than that recorded with the corresponding single $BiVO_4$ photoanodes with the same thickness of the $BiVO_4$ layer. The two types of photoanodes exhibit a photocurrent increasing with increasing $BiVO_4$ thickness for $BiVO_4$ thicknesses in the 15−75 nm range but a different behavior for a relatively higher $BiVO_4$ layer thickness. In fact, while in single $BiVO_4$ photoanodes, the photocurrent density increases with the $BiVO_4$ thickness up to 115 nm, and almost the same LSV curve is obtained with $BiVO_4$-115 and $BiVO_4$-160 (Figure 6A), in the case of the $WO_3/BiVO_4$ coupled system the highest photocurrent density is attained with $WO_3/BiVO_4$-75, having a 75 nm thick $BiVO_4$ layer, while progressively lower LSV curves are recorded with the thicker $WO_3/BiVO_4$-115 and the $WO_3/BiVO_4$-160 photoanodes (Figure 6B).

The PEC properties of the two series of electrodes were also investigated by IPCE tests at 1.23 V versus RHE in a Na_2SO_4 0.5 M electrolyte solution. The IPCE curves obtained under backside irradiation with all photoanodes, reported in Figure 7A,B, show that, in general, $BiVO_4$ is active up to 520 nm and that in pure $BiVO_4$ photoanodes (Figure 7A) the IPCE increases with the increasing thickness of the $BiVO_4$ layer, in line with the results of LSV analysis shown in Figure 6A.

On the other hand, all heterojunction electrodes (Figure 7B) outperform the IPCE of the thickest $BiVO_4$ film. Indeed, the charge separation occurring in the $WO_3/BiVO_4$ electrodes and the superior charge-transport properties of WO_3 with respect to $BiVO_4$ allow us to achieve a higher IPCE by limiting the charge-carrier recombination.[28,74,75] In this case, the IPCE increases with increasing $BiVO_4$ film thickness only for the thinner $BiVO_4$ layers in the composite system, the $WO_3/BiVO_4$-75 electrode exhibiting the highest efficiency (Figure 7B), while thicker $WO_3/BiVO_4$-115 and $WO_3/BiVO_4$-160 composite photoanodes become progressively less efficient at wavelengths below 450 nm. Also, these results are fully compatible with the results of LSV analyses shown in Figure 6B.

When photoanodes are irradiated from the FTO side, most of the charge carriers are photogenerated in $BiVO_4$ close to the WO_3 layer. In particular, the so-produced holes need to be transferred through the $BiVO_4$ layer to reach water molecules at the electrode/electrolyte interface. Along this way, they can recombine with photopromoted electrons trapped in $BiVO_4$, and the probability that they reach the electrode/electrolyte interface decreases with the increasing thickness of the $BiVO_4$ layer.

The wavelength dependence of the IPCE curves recorded with $WO_3/BiVO_4$ electrodes is consequent to the fact that the WO_3 layer absorbs light below 450 nm (see Figure 2B). Under

https://doi.org/10.1021/acsaem.1c01623
ACS Appl. Energy Mater. 2021, 4, 8421−8431

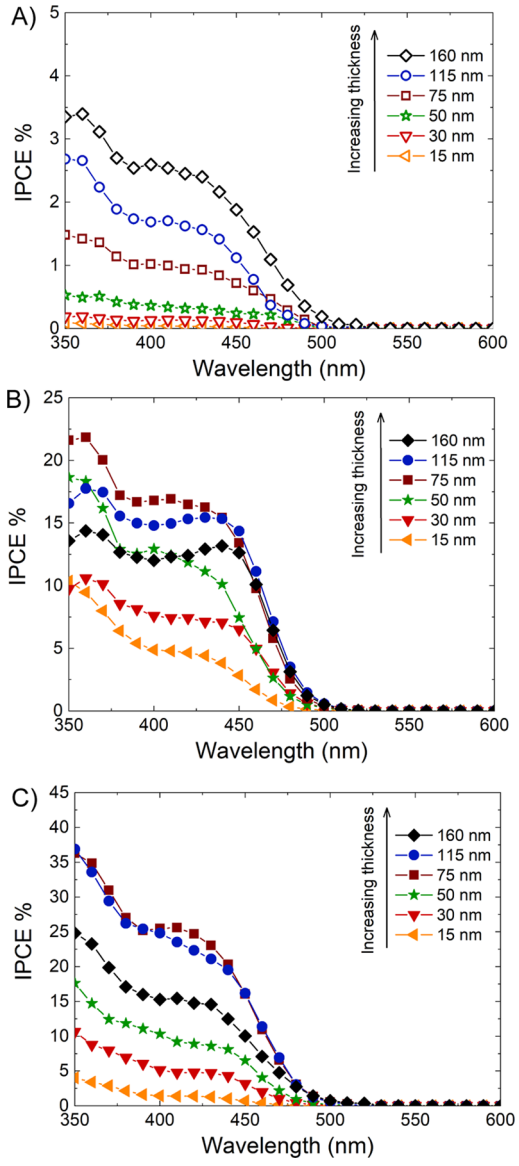

Figure 7. IPCE curves of (A) the $BiVO_4$ and (B) the $WO_3/BiVO_4$ photoanode series under backside irradiation and of (C) the $WO_3/BiVO_4$ photoanode series under frontside irradiation, recorded in Na_2SO_4 0.5 M aqueous solution under a 1.23 V vs RHE applied bias.

such conditions, the holes photogenerated in $BiVO_4$ close to the $WO_3/BiVO_4$ heterojunction may partly recombine with electrons photopromoted in the CB of WO_3, as demonstrated by ultrafast transient absorption measurements in our previous study.[63]

These effects become more evident with the increasing thickness of the $BiVO_4$ layer in $WO_3/BiVO_4$ photoanodes, producing a change in the shape of the IPCE curves (Figure 7B) with the relative photon-to-current efficiency at a shorter wavelength monotonously decreasing with increasing $BiVO_4$ layer thickness. Indeed, in the case of the $WO_3/BiVO_4$-15 photoanode, having the thinnest (15 nm thick) $BiVO_4$ layer so that holes are also photoproduced close to the electrode/electrolyte interface, the IPCE is by far maximum at the shortest wavelengths, though its average value is lower than in thicker photoanodes due to the lower amount of absorbed light.

The recombination between CB electrons in WO_3 and VB holes in $BiVO_4$ at the $WO_3/BiVO_4$ heterojunction becomes much less important if the electrodes are irradiated from the front side (through the $BiVO_4$/electrolyte interface). In fact, the IPCE curves recorded with the $WO_3/BiVO_4$ electrodes under frontside irradiation (Figure 7C) are almost doubled with respect to those recorded under backside irradiation (Figure 7B), with relatively higher IPCE values especially at wavelengths shorter than 450 nm and for coupled systems containing a $BiVO_4$ layer thicker than 50 nm, that is, under conditions of relatively low excitation of the WO_3 underlayer.

The heterojunction film with a $BiVO_4$ thickness of 75 nm presents (under both irradiation configurations) the optimal balance between visible light absorption and low charge-carrier recombination during hole transfer to the electrode/electrolyte interface, and this leads to maximum IPCE.

Finally, the much better performance of composite $WO_3/BiVO_4$-15 with respect to single $BiVO_4$-15 (Figure 6) confirms what predicted by DFT calculations, that is, the stabilization of a type-II heterojunction is able to promote an effective electron−hole separation in coupled $WO_3/BiVO_4$ systems with an at least 3 nm thick $BiVO_4$ layer.

4. CONCLUSIONS

In conclusion, we tuned the visible light absorption of the $WO_3/BiVO_4$ heterojunction by increasing the $BiVO_4$ thickness and observed that the WO_3 underlayer impacts the $BiVO_4$ crystal structure, in particular on the {010} plane. DFT calculations support that the two oxides are joint at the WO_3 {001} and $BiVO_4$ {010} interface and that the heterojunction leads to a type-II band alignment and a charge polarization, which are beneficial for charge separation. The observed wavelength-dependent PEC performance of the composite $WO_3/BiVO_4$ photoanodes with differently thick $BiVO_4$-coated layers results from the relatively poor charge-transport properties of the $BiVO_4$ layers and the probability that holes photoproduced in $BiVO_4$ close to the interface between the two oxides recombine with electrons photopromoted in the WO_3 CB upon irradiation at wavelengths below 450 nm. The $WO_3/BiVO_4$ electrode with a 75 nm thick $BiVO_4$ layer is best performing, with an optimal balance between thickness-dependent effective light absorption and charge-carrier recombination. These results deepen the insights into this heterojunction and may suggest a strategy to develop efficient visible-light-harvesting systems.

■ ASSOCIATED CONTENT

Supporting Information

The Supporting Information is available free of charge at https://pubs.acs.org/doi/10.1021/acsaem.1c01623.

Cross-sectional FESEM images and extinction coefficient of $BiVO_4$, supporting XRD analyses, and supporting DFT calculations (PDF)

■ AUTHOR INFORMATION

Corresponding Author

Elena Selli − *Dipartimento di Chimica, Università degli Studi di Milano, 20133 Milano, Italy;* orcid.org/0000-0001-8391-7639; Email: elena.selli@unimi.it

https://doi.org/10.1021/acsaem.1c01623
ACS Appl. Energy Mater. 2021, 4, 8421−8431

Authors

Ivan Grigioni − *Dipartimento di Chimica, Università degli Studi di Milano, 20133 Milano, Italy;* orcid.org/0000-0002-9469-4570

Giovanni Di Liberto − *Dipartimento di Scienza dei Materiali, Università di Milano-Bicocca, 20125 Milano, Italy;* orcid.org/0000-0003-4289-2732

Maria Vittoria Dozzi − *Dipartimento di Chimica, Università degli Studi di Milano, 20133 Milano, Italy;* orcid.org/0000-0002-6390-9348

Sergio Tosoni − *Dipartimento di Scienza dei Materiali, Università di Milano-Bicocca, 20125 Milano, Italy;* orcid.org/0000-0001-5700-4086

Gianfranco Pacchioni − *Dipartimento di Scienza dei Materiali, Università di Milano-Bicocca, 20125 Milano, Italy;* orcid.org/0000-0002-4749-0751

Complete contact information is available at: https://pubs.acs.org/10.1021/acsaem.1c01623

Author Contributions

[§]I.V. and G.D.L. contributed equally.

Notes

The authors declare no competing financial interest.

■ ACKNOWLEDGMENTS

This work received financial support from the MIUR PRIN 20173397R7 MULTI-e project, from the European Union's Horizon 2020 research and innovation programme under the Marie Sklodowska-Curie Grant no. 846107, and from a Transition Grant of the University of Milano. The use of instrumentation purchased through the Regione Lombardia-Fondazione Cariplo joint SmartMatLab project (Fondazione Cariplo grant 2013-1766) is also gratefully acknowledged. G.D.L., S.T., and G.P. also acknowledge the grant Dipartimenti di Eccellenza—2017 "Materials For Energy". Access to the CINECA supercomputing resources was granted via ISCRAB. We also thank the COST Action 18234 supported by COST (European Cooperation in Science and Technology).

■ REFERENCES

(1) Kim, J. H.; Hansora, D.; Sharma, P.; Jang, J.-W.; Lee, J. S. Toward Practical Solar Hydrogen Production - an Artificial Photosynthetic Leaf-to-Farm Challenge. *Chem. Soc. Rev.* **2019**, *48*, 1908−1971.

(2) Sivula, K.; Zboril, R.; Le Formal, F.; Robert, R.; Weidenkaff, A.; Tucek, J.; Frydrych, J.; Grätzel, M. Photoelectrochemical Water Splitting with Mesoporous Hematite Prepared by a Solution-Based Colloidal Approach. *J. Am. Chem. Soc.* **2010**, *132*, 7436−7444.

(3) Santato, C.; Odziemkowski, M.; Ulmann, M.; Augustynski, J. Crystallographically Oriented Mesoporous WO_3 Films: Synthesis, Characterization, and Applications. *J. Am. Chem. Soc.* **2001**, *123*, 10639−10649.

(4) Higashi, M.; Domen, K.; Abe, R. Fabrication of an Efficient $BaTaO_2N$ Photoanode Harvesting a Wide Range of Visible Light for Water Splitting. *J. Am. Chem. Soc.* **2013**, *135*, 10238−10241.

(5) Polo, A.; Nomellini, C.; Grigioni, I.; Dozzi, M. V.; Selli, E. Effective Visible Light Exploitation by Copper Molybdo-Tungstate Photoanodes. *ACS Appl. Energy Mater.* **2020**, *3*, 6956−6964.

(6) Lee, D. K.; Choi, K.-S. Enhancing Long-Term Photostability of $BiVO_4$ Photoanodes for Solar Water Splitting by Tuning Electrolyte Composition. *Nat. Energy* **2018**, *3*, 53−60.

(7) Kuang, Y.; Jia, Q.; Ma, G.; Hisatomi, T.; Minegishi, T.; Nishiyama, H.; Nakabayashi, M.; Shibata, N.; Yamada, T.; Kudo, A.; Domen, K. Ultrastable Low-Bias Water Splitting Photoanodes via Photocorrosion Inhibition and in Situ Catalyst Regeneration. *Nat. Energy* **2017**, *2*, 1−3.

(8) Abdi, F. F.; Han, L.; Smets, A. H. M.; Zeman, M.; Dam, B.; van de Krol, R. Efficient Solar Water Splitting by Enhanced Charge Separation in a Bismuth Vanadate-Silicon Tandem Photoelectrode. *Nat. Commun.* **2013**, *4*, 2195.

(9) Kim, T. W.; Choi, K.-S. Nanoporous $BiVO_4$ Photoanodes with Dual-Layer Oxygen Evolution Catalysts for Solar Water Splitting. *Science* **2014**, *343*, 990−994.

(10) Abdi, F. F.; van de Krol, R. Nature and Light Dependence of Bulk Recombination in Co-Pi-Catalyzed $BiVO_4$ Photoanodes. *J. Phys. Chem. C* **2012**, *116*, 9398−9404.

(11) Zhou, S.; Chen, K.; Huang, J.; Wang, L.; Zhang, M.; Bai, B.; Liu, H.; Wang, Q. Preparation of Heterometallic CoNi-MOFs-Modified $BiVO_4$: A Steady Photoanode for Improved Performance in Photoelectrochemical Water Splitting. *Appl. Catal. B Environ.* **2020**, *266*, 118513.

(12) Pilli, S. K.; Furtak, T. E.; Brown, L. D.; Deutsch, T. G.; Turner, J. a.; Herring, A. M. Cobalt-Phosphate (Co-Pi) Catalyst Modified Mo-Doped $BiVO_4$ Photoelectrodes for Solar Water Oxidation. *Energy Environ. Sci.* **2011**, *4*, 5028−5034.

(13) Liang, Y.; Tsubota, T.; Mooij, L. P. A.; van de Krol, R. Highly Improved Quantum Efficiencies for Thin Film $BiVO_4$ Photoanodes. *J. Phys. Chem. C* **2011**, *115*, 17594−17598.

(14) Meng, Q.; Zhang, B.; Fan, L.; Liu, H.; Valvo, M.; Edström, K.; Cuartero, M.; Marco, R.; Crespo, G. A.; Sun, L. Efficient $BiVO_4$ Photoanodes by Postsynthetic Treatment: Remarkable Improvements in Photoelectrochemical Performance from Facile Borate Modification. *Angew. Chem.* **2019**, *131*, 19203−19209.

(15) Yin, X.; Qiu, W.; Li, W.; Li, C.; Wang, K.; Yang, X.; Du, L.; Liu, Y.; Li, J. High Porosity Mo Doped $BiVO_4$ Film by Vanadium Re-Substitution for Efficient Photoelectrochemical Water Splitting. *Chem. Eng. J.* **2020**, *389*, 124365.

(16) Wang, G.; Ling, Y.; Lu, X.; Qian, F.; Tong, Y.; Zhang, J. Z.; Lordi, V.; Rocha Leao, C.; Li, Y. Computational and Photoelectrochemical Study of Hydrogenated Bismuth Vanadate. *J. Phys. Chem. C* **2013**, *117*, 10957−10964.

(17) Hong, S. J.; Lee, S.; Jang, J. S.; Lee, J. S. Heterojunction $BiVO_4$/WO_3 Electrodes for Enhanced Photoactivity of Water Oxidation. *Energy Environ. Sci.* **2011**, *4*, 1781−1787.

(18) Shi, X.; Jeong, H.; Oh, S. J.; Ma, M.; Zhang, K.; Kwon, J.; Choi, I. T.; Choi, I. Y.; Kim, H. K.; Kim, J. K.; Park, J. H. Unassisted Photoelectrochemical Water Splitting Exceeding 7% Solar-to-Hydrogen Conversion Efficiency Using Photon Recycling. *Nat. Commun.* **2016**, *7*, 11943.

(19) Pihosh, Y.; Turkevych, I.; Mawatari, K.; Uemura, J.; Kazoe, Y.; Kosar, S.; Makita, K.; Sugaya, T.; Matsui, T.; Fujita, D.; Tosa, M.; Kondo, M.; Kitamori, T. Photocatalytic Generation of Hydrogen by Core-Shell WO_3/$BiVO_4$ Nanorods with Ultimate Water Splitting Efficiency. *Sci. Rep.* **2015**, *5*, 11141.

(20) Xu, S.; Fu, D.; Song, K.; Wang, L.; Yang, Z.; Yang, W.; Hou, H. One-Dimensional WO_3/$BiVO_4$ Heterojunction Photoanodes for Efficient Photoelectrochemical Water Splitting. *Chem. Eng. J.* **2018**, *349*, 368−375.

(21) Ma, Z.; Hou, H.; Song, K.; Fang, Z.; Wang, L.; Gao, F.; Yang, Z.; Tang, B.; Yang, W. Ternary WO_3/Porous-$BiVO_4$/FeOOH Hierarchical Architectures: Towards Highly Efficient Photoelectrochemical Performance. *ChemElectroChem* **2018**, *5*, 3660−3667.

(22) Ma, Z.; Song, K.; Wang, L.; Gao, F.; Tang, B.; Hou, H.; Yang, W. WO_3/$BiVO_4$ Type-II Heterojunction Arrays Decorated with Oxygen-Deficient ZnO Passivation Layer: A Highly Efficient and Stable Photoanode. *ACS Appl. Mater. Interfaces* **2019**, *11*, 889−897.

(23) Grigioni, I.; Ganzer, L.; Camargo, F. V. A.; Bozzini, B.; Cerullo, G.; Selli, E. In Operando Photoelectrochemical Femtosecond Transient Absorption Spectroscopy of WO_3/$BiVO_4$ Heterojunctions. *ACS Energy Lett.* **2019**, *4*, 2213−2219.

(24) Selim, S.; Francàs, L.; García-Tecedor, M.; Corby, S.; Blackman, C.; Gimenez, S.; Durrant, J. R.; Kafizas, A. WO_3/$BiVO_4$:

Impact of Charge Separation at the Timescale of Water Oxidation. *Chem. Sci.* **2019**, *10*, 2643−2652.
(25) Grigioni, I.; Stamplecoskie, K. G.; Selli, E.; Kamat, P. V. Dynamics of Photogenerated Charge Carriers in WO_3/$BiVO_4$ Heterojunction Photoanodes. *J. Phys. Chem. C* **2015**, *119*, 20792−20800.
(26) Abdi, F. F.; Savenije, T. J.; May, M. M.; Dam, B.; van de Krol, R. The Origin of Slow Carrier Transport in $BiVO_4$ Thin Film Photoanodes: A Time-Resolved Microwave Conductivity Study. *J. Phys. Chem. Lett.* **2013**, *4*, 2752−2757.
(27) Grigioni, I.; Abdellah, M.; Corti, A.; Dozzi, M. V.; Hammarström, L.; Selli, E. Photoinduced Charge-Transfer Dynamics in WO_3/$BiVO_4$ Photoanodes Probed through Midinfrared Transient Absorption Spectroscopy. *J. Am. Chem. Soc.* **2018**, *140*, 14042−14045.
(28) Grigioni, I.; Dozzi, M. V.; Selli, E. Photoinduced Electron Transfer in WO_3/$BiVO_4$ Heterojunction Photoanodes: Effects of the WO_3 Layer Thickness. *J. Phys.: Condens. Matter* **2020**, *32*, 014001.
(29) Ma, Y.; Kafizas, A.; Pendlebury, S. R.; Le Formal, F.; Durrant, J. R. Photoinduced Absorption Spectroscopy of CoPi on $BiVO_4$: The Function of CoPi during Water Oxidation. *Adv. Funct. Mater.* **2016**, *26*, 4951−4960.
(30) Ma, Y.; Pendlebury, S. R.; Reynal, A.; Le Formal, F.; Durrant, J. R. Dynamics of Photogenerated Holes in Undoped $BiVO_4$ Photoanodes for Solar Water Oxidation. *Chem. Sci.* **2014**, *5*, 2964−2973.
(31) Ravensbergen, J.; Abdi, F. F.; Van Santen, J. H.; Frese, R. N.; Dam, B.; Van De Krol, R.; Kennis, J. T. M. Unraveling the Carrier Dynamics of $BiVO_4$: A Femtosecond to Microsecond Transient Absorption Study. *J. Phys. Chem. C* **2014**, *118*, 27793−27800.
(32) Loiudice, A.; Cooper, J. K.; Hess, L. H.; Mattox, T. M.; Sharp, I. D.; Buonsanti, R. Assembly and Photocarrier Dynamics of Heterostructured Nanocomposite Photoanodes from Multicomponent Colloidal Nanocrystals. *Nano Lett.* **2015**, *15*, 7347−7354.
(33) Liu, Y.; Wygant, B. R.; Kawashima, K.; Mabayoje, O.; Hong, T. E.; Lee, S.-G.; Lin, J.; Kim, J.-H.; Yubuta, K.; Li, W.; Li, J.; Mullins, C. B. Facet Effect on the Photoelectrochemical Performance of a WO_3/$BiVO_4$ Heterojunction Photoanode. *Appl. Catal. B Environ.* **2019**, *245*, 227−239.
(34) Su, J.; Guo, L.; Yoriya, S.; Grimes, C. A. Aqueous Growth of Pyramidal-Shaped $BiVO_4$ Nanowire Arrays and Structural Characterization: Application to Photoelectrochemical Water Splitting. *Cryst. Growth Des.* **2010**, *10*, 856−861.
(35) Dovesi, R.; Erba, A.; Orlando, R.; Zicovich-Wilson, C. M.; Civalleri, B.; Maschio, L.; Rérat, M.; Casassa, S.; Baima, J.; Salustro, S.; Kirtman, B. Quantum-Mechanical Condensed Matter Simulations with CRYSTAL. *Wiley Interdiscip. Rev.: Comput. Mol. Sci.* **2018**, *8*, No. e1360.
(36) Heyd, J.; Scuseria, G. E.; Ernzerhof, M. Hybrid Functionals Based on a Screened Coulomb Potential. *J. Chem. Phys.* **2003**, *118*, 8207−8215.
(37) Heyd, J.; Peralta, J. E.; Scuseria, G. E.; Martin, R. L. Energy Band Gaps and Lattice Parameters Evaluated with the Heyd-Scuseria-Ernzerhof Screened Hybrid Functional. *J. Chem. Phys.* **2005**, *123*, 174101.
(38) Das, T.; Di Liberto, G.; Tosoni, S.; Pacchioni, G. Band Gap of 3D Metal Oxides and Quasi-2D Materials from Hybrid Density Functional Theory: Are Dielectric-Dependent Functionals Superior? *J. Chem. Theory Comput.* **2019**, *15*, 6294−6312.
(39) Ruiz, E.; Llunell, M.; Alemany, P. Calculation of Exchange Coupling Constants in Solid State Transition Metal Compounds Using Localized Atomic Orbital Basis Sets. *J. Solid State Chem.* **2003**, *176*, 400−411.
(40) Wadt, W. R.; Hay, P. J. Ab Initio Effective Core Potentials for Molecular Calculations. Potentials for Main Group Elements Na to Bi. *J. Chem. Phys.* **1985**, *82*, 284−298.
(41) Hay, P. J.; Wadt, W. R. Ab Initio Effective Core Potentials for Molecular Calculations. Potentials for the Transition Metal Atoms Sc to Hg. *J. Chem. Phys.* **1985**, *82*, 270−283.
(42) Wang, F.; Di Valentin, C.; Pacchioni, G. Electronic and Structural Properties of WO_3: A Systematic Hybrid DFT Study. *J. Phys. Chem. C* **2011**, *115*, 8345−8353.
(43) Wang, F.; Di Valentin, C.; Pacchioni, G. DFT Study of Hydrogen Adsorption on the Monoclinic WO_3 (001) Surface. *J. Phys. Chem. C* **2012**, *116*, 10672−10679.
(44) Di Liberto, G.; Tosoni, S.; Pacchioni, G. Theoretical Treatment of Semiconductor Heterojunctions for Photocatalysis: The WO_3/$BiVO_4$ Interface. *J. Phys.: Condens. Matter* **2019**, *31*, 434001.
(45) Vilela Oliveira, D.; Laun, J.; Peintinger, M. F.; Bredow, T. BSSE-correction Scheme for Consistent Gaussian Basis Sets of Double- and Triple-zeta Valence with Polarization Quality for Solid-state Calculations. *J. Comput. Chem.* **2019**, *40*, 2364−2376.
(46) Wang, W.; Strohbeen, P. J.; Lee, D.; Zhou, C.; Kawasaki, J. K.; Choi, K.-S.; Liu, M.; Galli, G. The Role of Surface Oxygen Vacancies in $BiVO_4$. *Chem. Mater.* **2020**, *32*, 2899−2909.
(47) Conesa, J. C. Modeling with Hybrid Density Functional Theory the Electronic Band Alignment at the Zinc Oxide-Anatase Interface. *J. Phys. Chem. C* **2012**, *116*, 18884−18890.
(48) Di Paola, A.; Palmisano, L.; Venezia, A. M.; Augugliaro, V.; Ugo, V.; Malfa, L. Coupled Semiconductor Systems for Photocatalysis. Preparation and Characterization of Polycrystalline Mixed WO_3/WS_2 Powders. *J. Phys. Chem. B* **1999**, *103*, 8236−8244.
(49) Su, J.; Guo, L.; Bao, N.; Grimes, C. A. Nanostructured WO_3/$BiVO_4$ Heterojunction Films for Efficient Photoelectrochemical Water Splitting. *Nano Lett.* **2011**, *11*, 1928−1933.
(50) Zhao, Z.; Li, Z.; Zou, Z. Structure and Energetics of Low-Index Stoichiometric Monoclinic Clinobisvanite $BiVO_4$ Surfaces. *RSC Adv.* **2011**, *1*, 874−883.
(51) Di Liberto, G.; Tosoni, S.; Pacchioni, G. Role of Surface Termination in Forming Type-II Photocatalyst Heterojunctions: The Case of TiO_2/$BiVO_4$. *J. Phys.: Condens. Matter* **2021**, *33*, 075001.
(52) Li, R.; Zhang, F.; Wang, D.; Yang, J.; Li, M.; Zhu, J.; Zhou, X.; Han, H.; Li, C. Spatial Separation of Photogenerated Electrons and Holes among {010} and {110} Crystal Facets of $BiVO_4$. *Nat. Commun.* **2013**, *4*, 1432.
(53) Samsudin, M. F. R.; Ullah, H.; Bashiri, R.; Mohamed, N. M.; Sufian, S.; Ng, Y. H. Experimental and DFT Insights on Microflower G-C_3N_4/$BiVO_4$ Photocatalyst for Enhanced Photoelectrochemical Hydrogen Generation from Lake Water. *ACS Sustainable Chem. Eng.* **2020**, *8*, 9393−9403.
(54) Uedono, A.; Shimayama, K.; Kiyohara, M.; Chen, Z. Q.; Yamabe, K. Study of Oxygen Vacancies in $SrTiO_3$ by Positron Annihilation. *J. Appl. Phys.* **2002**, *92*, 2697−2702.
(55) Loopstra, B. O.; Rietveld, H. M. Further Refinement of the Structure of WO_3. *Acta Crystallogr., Sect. B: Struct. Crystallogr. Cryst. Chem.* **1969**, *25*, 1420−1421.
(56) Sleight, A. W.; Chen, H.-y.; Ferretti, A.; Cox, D. E. Crystal Growth and Structure of $BiVO_4$. *Mater. Res. Bull.* **1979**, *14*, 1571−1581.
(57) Liu, J.-C.; Chen, J.-P.; Li, D.-Y. Crystal Structure and Optical Observations of $BiVO_4$. *Wuli Xuebao* **1983**, *32*, 1053.
(58) Li, G.-L. First-Principles Investigation of the Surface Properties of Fergusonite -Type Monoclinic $BiVO_4$ Photocatalyst. *RSC Adv.* **2017**, *7*, 9130−9140.
(59) Zhao, Z.; Li, Z.; Zou, Z. Electronic Structure and Optical Properties of Monoclinic Clinobisvanite $BiVO_4$. *Phys. Chem. Chem. Phys.* **2011**, *13*, 4746−4753.
(60) Butler, K. T.; Sai Gautam, G.; Canepa, P. Designing Interfaces in Energy Materials Applications with First-Principles Calculations. *npj Comput. Mater.* **2019**, *5*, 19.
(61) Di Liberto, G.; Tosoni, S.; Pacchioni, G. Nature and Role of Surface Junctions in $BiOIO_3$ Photocatalysts. *Adv. Funct. Mater.* **2021**, *31*, 2009472.
(62) Hutchins, M. G.; Abu-Alkhair, O.; El-Nahass, M. M.; El-Hady, K. A. Structural and Optical Characterisation of Thermally Evaporated Tungsten Trioxide (WO_3) Thin Films. *Mater. Chem. Phys.* **2006**, *98*, 401−405.

https://doi.org/10.1021/acsaem.1c01623
ACS Appl. Energy Mater. 2021, 4, 8421−8431

(63) Laraib, I.; Carneiro, M. A.; Janotti, A. Effects of Doping on the Crystal Structure of $BiVO_4$. *J. Phys. Chem. C* **2019**, *123*, 26752−26757.
(64) Xu, Q.; Zhang, L.; Yu, J.; Wageh, S.; Al-Ghamdi, A. A.; Jaroniec, M. Direct Z-Scheme Photocatalysts: Principles, Synthesis, and Applications. *Mater. Today* **2018**, *21*, 1042−1063.
(65) Liu, J.; Hua, E. High Photocatalytic Activity of Heptazine-Based g-C_3N_4/SnS_2 Heterojunction and Its Origin: Insights from Hybrid DFT. *J. Phys. Chem. C* **2017**, *121*, 25827−25835.
(66) Di Liberto, G.; Tosoni, S.; Pacchioni, G. Nitrogen Doping in Coexposed (001)−(101) Anatase TiO_2 Surfaces: A DFT Study. *Phys. Chem. Chem. Phys.* **2019**, *21*, 21497−21505.
(67) Van de Walle, C. G.; Martin, R. M. Theoretical Study of Band Offsets at Semiconductor Interfaces. *Phys. Rev. B: Condens. Matter Mater. Phys.* **1987**, *35*, 8154−8165.
(68) Low, J.; Yu, J.; Jaroniec, M.; Wageh, S.; Al-Ghamdi, A. A. Heterojunction Photocatalysts. *Adv. Mater.* **2017**, *29*, 1601694.
(69) Wang, H.; Zhang, L.; Chen, Z.; Hu, J.; Li, S.; Wang, Z.; Liu, J.; Wang, X. Semiconductor Heterojunction Photocatalysts: Design, Construction, and Photocatalytic Performances. *Chem. Soc. Rev.* **2014**, *43*, 5234.
(70) Di Liberto, G.; Tosoni, S.; Pacchioni, G. Role of Heterojunction in Charge Carrier Separation in Coexposed Anatase (001)-(101) Surfaces. *J. Phys. Chem. Lett.* **2019**, *10*, 2372−2377.
(71) Liu, C.; Yang, Y.; Li, J.; Chen, S.; Li, W.; Tang, X. An in Situ Transformation Approach for Fabrication of $BiVO_4$/WO_3 Heterojunction Photoanode with High Photoelectrochemical Activity. *Chem. Eng. J.* **2017**, *326*, 603−611.
(72) Conesa, J. C. Computing with DFT Band Offsets at Semiconductor Interfaces: A Comparison of Two Methods. *Nanomaterials* **2021**, *11*, 1581.
(73) Cipriano, L. A.; Di Liberto, G.; Tosoni, S.; Pacchioni, G. Quantum Confinement in Group III−V Semiconductor 2D Nanostructures. *Nanoscale* **2020**, *12*, 17494−17501.
(74) Grigioni, I.; Stamplecoskie, K. G.; Jara, D. H.; Dozzi, M. V.; Oriana, A.; Cerullo, G.; Kamat, P. V.; Selli, E. Wavelength-Dependent Ultrafast Charge Carrier Separation in the WO_3/$BiVO_4$ Coupled System. *ACS Energy Lett.* **2017**, *2*, 1362−1367.
(75) Polo, A.; Grigioni, I.; Dozzi, M. V.; Selli, E. Sensitizing Effects of $BiVO_4$ and Visible Light Induced Production of Highly Reductive Electrons in the TiO_2/$BiVO_4$ Heterojunction. *Catal. Today* **2020**, *340*, 19−25.

https://doi.org/10.1021/acsaem.1c01623
ACS Appl. Energy Mater. 2021, 4, 8421−8431